Narrow, fast, and "cool" mantle plumes caused by strain-weakening rheology in Earth's lower mantle

Anna J. P. Gülcher[1], G. J. Golabek[2], M. Thielmann[2], M. D. Ballmer[3], and P. J. Tackley[1]

[1]Institute of Geophysics, Department of Earth Sciences, ETH Zurich, Zurich, Switzerland
[2]Bayerisches Geoinstitut, University Bayreuth, Bayreuth, Germany
[3]UCL Earth Sciences, University College London, London, UK

Published in: Geochemistry, Geophysics, Geosystems, 23, e2021GC010314 (2022)

Link: **https://doi.org/10.1029/2021GC010314**

Note: this is a post-script of the article

Key Points:

- A new strain-weakening (SW) rheology for lower mantle materials is implemented in numerical models of global-scale mantle convection
- Such rheology causes weakening of plume conduits, forming narrow lubrication channels in the mantle through which hot material easily rises
- SW rheology in the lower mantle could explain the discrepancy between expected and observed thermal anomalies of deep mantle plumes on Earth

Corresponding author: Anna Gülcher, anna.guelcher@erdw.ethz.ch

Abstract

The rheological properties of Earth's lower mantle are key for mantle dynamics and planetary evolution. The main rock-forming minerals in the lower mantle are bridgmanite (Br) and smaller amounts of ferropericlase (Fp). Previous work has suggested that the large differences in viscosity between these minerals greatly affect the bulk rock rheology. The resulting effective rheology becomes highly strain-dependent as weaker Fp minerals become elongated and eventually interconnected. This implies that strain localization may occur in Earth's lower mantle. So far, there have been no studies on global-scale mantle convection in the presence of such strain-weakening (SW) rheology. Here, we present 2D numerical models of thermo-chemical convection in spherical annulus geometry including a new strain-dependent rheology formulation for lower mantle materials, combining rheological weakening and healing terms. We find that SW rheology has several direct and indirect effects on mantle convection. The most notable direct effect is the changing dynamics of weakened plume channels as well as the formation of larger thermochemical piles at the base of the mantle. The weakened plume conduits act as lubrication channels in the mantle and exhibit a lower thermal anomaly. SW rheology also reduces the overall viscosity, notable in terms of increasing convective vigor and core-mantle boundary (CMB) heat flux. Finally, we put our results into context with existing hypotheses on the style of mantle convection and mixing. Most importantly, we suggest that the new kind of plume dynamics may explain the discrepancy between expected and observed thermal anomalies of deep-seated mantle plumes on Earth.

Plain Language Summary

Earth's lower mantle (660-2890 km depth) controls our planet's evolution by regulating the transport of materials and heat through mantle convection. To better understand mantle convection and the evolution of Earth over billions of years, mathematical laws describing how rocks flow (viscosity) are needed. Recently, it was discovered that the deformation history of lower-mantle rocks affects the viscosity. In the lower mantle there are two main minerals: Bridgmanite (Br), which is relatively strong (high viscosity), and ferropericlase (Fp), which is relatively weak (low viscosity). When a rock containing both minerals is deformed, the weak Fp grains can form interconnected layers, lowering the overall viscosity and thus weakening the whole rock.

Here, we present prompting new results that show how mantle convection and Earth's evolution are affected by such a deformation-dependent or "strain-weakening" (SW) viscosity law, using global-scale numerical simulations of mantle convection and plate tectonics. We find that, in particular, the dynamics of hot, rising columns of mantle material (plumes) are affected by SW rheology, making them more narrow, fast, and less hot relatively to other plumes. Finally, we find that this new types of plume dynamics could be linked to several observations of mantle plumes in the Earth.

1 Introduction

Solid-state convection of the rocky, 2890-km deep mantle shapes the evolution of Earth's interior and surface over billions of years. The style of mantle convection and its temporal evolution is therefore subject to active research. At least in the lower mantle, Earth's convective system is dominated by a degree-2 pattern, with two broad, antipodal, equatorial regions of upwellings surrounded by sheets of downwellings. The convective system is further characterised by existence of several geochemically distinct (and perhaps long-term isolated) reservoirs within (e.g., Garnero & McNamara, , ,). The two large low shear-wave velocity piles (LLSVP) in Earth's lowermost mantle spatially correlate with the two antipodal upwelling regions, and their edges seem to match with hotspot locations at the surface (Torsvik et al., ,). Since plumes can serve as an absolute reference frame for plate reconstructions (e.g., Wilson,), their temporal stability at their root and any deflections during upwelling are important to establish. Even though mantle plumes are an intrinsic part of Earth's convection system, their dynamics, geometries, and fixity remain poorly understood since they were first proposed (Morgan,).

To date, it is understood that mantle plumes can start as deep as the core–mantle boundary and rise all the way to the base of the lithosphere, where they sustain intraplate hotspot volcanism (Morgan,). In the classical view (Howard, ,), a rising mantle plume is characterized by a large head atop a narrow tail, although chemical complexities may result in deviations from such classical shapes (Farnetani & Samuel, , ,). Plume shapes are difficult to clearly be imaged by seismic tomography due to wavefront healing (Ritsema et al.,). Although recent full-waveform tomography models hint at the presence of plume-like features associated with major hotspots (e.g. French & Romanowicz,), ambiguity remains as to the vertical continuity of these features, as well as their shapes and stability (e.g., Wolfe et al., , ,). Another controversy lies in the temperature excess of such mantle plumes. Based on petrologic thermo-barometry, excess temperatures of plumes have been estimated at 100-300 K (Boehler,), with even lower estimates based on seismic observations (30-150 K, Bao et al.,). Both these estimated ranges are significantly lower than the expected CMB temperature difference of $\sim$1000 K. While the dynamics and shapes of plumes are well studied in geodynamic models with Newtonian rheology, they strongly depend on the material properties of mantle rocks (e.g. Massmeyer et al.,). However, these properties, and in particular the rheology of the lower mantle, are ill-constrained.

The two main constituents of the lower mantle are bridgmanite (Br) and ferropericlase (Fp) (Hirose, Morard, et al.,). The viscosity of the strong mineral bridgmanite ($\eta_{\mathrm{Br}} = 10^{21} - 10^{23}$ Pa·s) is several orders of magnitude larger than that of the weak ferropericlase ($\eta_{\mathrm{Fp}} = 10^{18}$–$10^{21}$ Pa·s) (Yamazaki & Karato, ,). It has been suggested that for typical mantle rocks that comprise Br as well as Fp, the bulk viscosity of the rock decreases with ongoing deformation as the weaker ferropericlase crystals become elongated in the direction of strain and interconnect with each other (Girard et al.,) (see Fig. 1a). This experimental result was further confirmed in numerical studies on the effective rheology of a lower-mantle two-phase medium during deformation (e.g., Thielmann et al., ,). The weakening of the bulk rock with accumulating strain ("strain weakening") implies that deformation may localize in the lower mantle, analogous to localized shear zones in crustal rocks. Such strain localization may potentially explain the isolation of large unmixed domains in the lower mantle, which may host primordial (or "hidden") geochemical reservoirs away from regions of localized deformation (Chen, , , ,) (see Fig. 1b). However, the effects of strain weakening on lower-mantle convection patterns and mixing dynamics have not yet been studied using global-scale geodynamic models.

Here, we implement a macro-scale description of strain-weakening (SW) rheology in a global mantle convection model. We present 2D numerical models of thermochemical convection in a spherical annulus geometry that include a new implementation of tracking the strain ellipse at each tracer through time. We allow lower mantle materials to rheologically weaken to various degrees and investigate the effects of this rheological weakening on mantle convection dynamics. We particularly focus on the characteristics of mantle plumes in the models. We find that SW rheology has several effects on mantle dynamics, including on the *(i)* pattern of mantle flow, *(ii)* thermal evolution of the mantle, *(iii)* pile stability, and *(iv)* mantle plume dynamics. We distinguish first-order effects (directly caused by spatial viscosity variations resulting from SW rheology) and second-order effects (indirectly caused by a changing Rayleigh number of the ambient mantle caused by SW), and link the results to the previously-proposed style of mantle convection (Fig. 1b). The changing plume dynamics are of particular interest since weak-

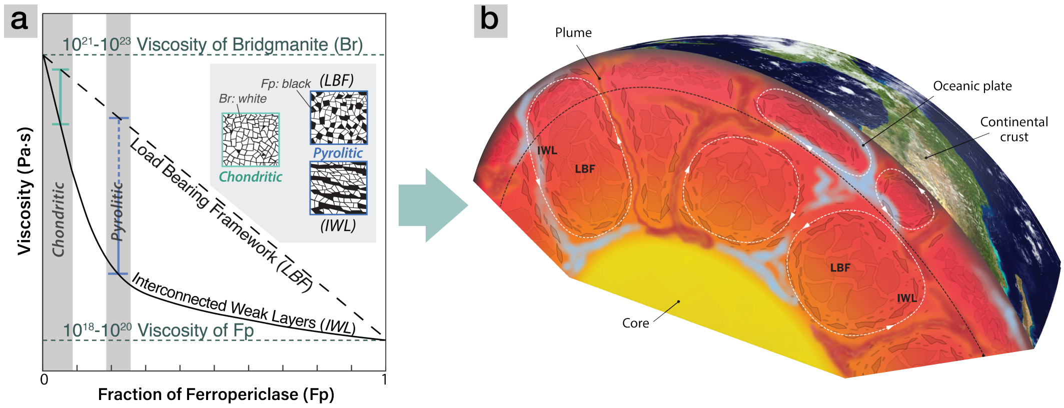

Figure 1. **(a)** Variation of the bulk viscosity of Br-Fp mixtures as a function of Fp fraction for the two end-member textures of "load-bearing framework" (LBF) and non-linear "interconnected weak layers" (IWL) (Handy,). Image adapted from Ballmer et al. (). **(b)** Suggested mantle convection dynamics in which shear localization of weak Fp grains induces weak layers of "interconnected frameworks" (IWL) along slabs and plumes, and mixing is less efficient for the bridgmanitic "load-bearing framework" (LBF) part of the lower mantle, potentially promoting the preservation of long-lived geochemical reservoirs. Reprinted from Chen (), Copyright (2016), with permission from The American Association for the Advancement of Science (AAAS).

ened plumes could explain the discrepancy between expected and observed thermal anomalies of deep-seated mantle plumes on Earth.

2 Methods

2.1 Numerical technique and model set-up

In this study, we use the finite-volume code StagYY (Tackley,) to model mantle convection in two-dimensional spherical annulus geometry (Hernlund & Tackley,) for 5 Gyrs of model time. The conservation equations for mass, momentum, energy and composition are solved on a staggered grid for a compressible fluid with an infinite Prandtl number (find full description of these equations in e.g. Tackley,). In the energy conservation, we include contributions of adiabatic, latent, and shear heating, but ignore radiogenic heating (see below). The computational domain is discretized by 1024×128 cells, in which $\sim$2.5 million tracers, tracking composition, temperature, and strain, are advected (20 tracers per cell). Due to vertical grid refinement near the boundary layers and near 660 km depth, the size of grid cells varies between 4 and 25 km in the vertical direction. Free-slip and isothermal boundary conditions are employed at the top and bottom boundaries, with a fixed surface temperature of 300 K and CMB temperature of 4000 K. The numerical experiments are purely bottom heated (i.e., no internal heating and constant core temperatures).

Initial mantle temperatures are calculated from an adiabat with a potential temperature of 1900 K, together with the top and bottom boundary layers, and superimposing small random temperature perturbations of $\pm$10 K on the cell level. The resulting temperature profile is $\sim$300 K warmer than Earth's present-day geotherm. Such increased initial mantle temperatures are applied to crudely mimic the thermal evolution of the mantle (especially since our models are purely bottom-heated), with higher convective vigor and widespread near-surface melting in the early model evolution (e.g., Davies, ,). Most modelled mantles in this study cool down to $\sim$1600-1650 K, consistent with

Depth [km]	**Temperature** [K]	$\triangle\rho_{\mathrm{pc}}$ [kg/m^3]	**Phase change width** [km]	γ [MPa/K]	K_0 [GPa]; K_0' [GPa/GPa]	**depth range** [km]
	Olivine ($\rho_{\mathrm{surf}} = 3240\ kg/m^3$)				163; 3.9	0-410
410	1600	180	discontinuous	+2.5	85; 3.9	410-660
660	1900	435	discontinuous	-2.5	210; 4.0	660-2740
2740	2300	61.6	25	+10	210; 4.0	2740-2890
	Pyroxene-garnet ($\rho_{\mathrm{surf}} = 3080\ kg/m^3$)				163; 3.9	0-40
40	1000	350	25	0	130; 3.9	40-300
300	1600	100	75	+1.0	85; 3.9	300-720
720	1900	350	75	+1.0	210; 4.0	720-2740
2740	2300	61.6	25	+10	210; 4.0	2740-2890

Table 1. Phase change parameters used in this study for the olivine and pyroxene-garnet systems. The table shows the depth and temperature at which a phase transition occurs; $\triangle\rho_{\mathrm{pc}}$ and γ denote the density jump across the phase transition and the Clapeyron slope, respectively. The Clapeyron slopes for these phase changes are similar to those used in previous numerical studies (e.g., Tackley et al.,). In the olivine system, the 410 and 660 phase changes are made discontinuous, whereas all other phase changes in all systems are defined as hyperbolic tangent functions (*tanh*) that transition between the phases across a predefined phase loop width. Finally, K_0 refers to the reference bulk modulus for the system for each individual layer (marked by the depth range), and K_0' refers to its pressure-derivative. The reference profiles of density, thermal expansivity, thermal conductivity, and specific heat of modelled mantle materials are given in Figure S3.

petrological studies on Earth's mantle temperatures over time (Herzberg & Rudnick,).

2.2 Treatment of mantle composition, phase changes and melting

The driving forces of mantle convection are related to rock density, which depends on temperature and composition (Nakagawa & Buffett, ,). Composition in our modelled mantle has two lithological end-member components: harzburgite and basalt, which are each treated as a mixture of olivine and pyroxene–garnet systems that undergo different solid-solid phase transitions (for details, see Nakagawa et al.,). Harzburgite is considered to be a mixture of 75% olivine and 25% pyroxene-garnet; basalt is considered as pure pyroxene-garnet (see their phase change parameters in Table 1). Each tracer carries a mechanical mixture of harzburgite and basalt, initially set to 80% harzburgite and 20% basalt (i.e., pyrolitic composition). The density profiles of harzburgite and MORB are consistent with those from (Xu et al.,), and they are plotted in Figure S3. Compositional anomalies carried on tracers evolve from the initial state due to melt-induced differentiation: they undergo partial melting as a function of pressure, temperature and composition to sustain the formation of basaltic crust, and leaving a harzburgitic residue (for details, see Nakagawa et al.,).

2.3 Visco-plastic rheology

Viscosity is temperature-, pressure-, composition- (or phase-), and strain-dependent following an Arrhenius-type viscosity law (Newtonian rheology):

$$\eta(T,P,c) = \eta_0 \cdot \lambda_{\mathrm{c}} \cdot f_{\mathrm{w}} \cdot exp\left(\frac{E_{\mathrm{a}} + P \cdot V_{\mathrm{a}}}{R \cdot T} - \frac{E_{\mathrm{a}}}{R \cdot T_0}\right) \tag{1}$$

Property	**Symbol**	**Value**	**Units**
Mantle domain thickness	D	2890	km
Gravitational acceleration	g	9.81	m/s^2
Surface temperature	T_s	300	K
CMB temperature	T_CMB	4000	K
Reference viscosity	η_0	$5{\cdot}10^{20}$	Pa·s
PV viscosity contrast	λ_pv	10	
PPV viscosity contrast	λ_ppv	10^{-3}	
Reference temperature	T_0	1600	K
Initial potential temperature	$T_{0,\mathrm{ini}}$	1900	K
Activation energy	E_a	200	kJ/mol
Activation energy - PPV	$E_\mathrm{a,PPV}$	100	kJ/mol
Activation volume	V_a	$2.6{\cdot}10^{-6}$	m^3/mol
Activation volume - PPV	$V_\mathrm{a,PPV}$	$1.0{\cdot}10^{-6}$	m^3/mol
Surface yield stress	τ_yield	30	MPa
Yield stress depth derivative	τ'_yield	0.01	MPa/MPa
Specific heat capacity	$C_\mathrm{P,0}$	1200	J/(kg·K)
Surface thermal conductivity	k_0	3	W/(m·K)
Surface thermal expansivity	α_0	$3{\cdot}10^{-5}$	K^{-1}

Table 2. Physical properties used in the simulations of this study. PV = perovskite; PPV = post-perovskite. Since we solve for compressible convection, the adiabatic temperature, density, thermal conductivity, and heat expansivity are pressure-dependent following a third-order Birch-Murnaghan equation of state (Tackley et al.,). The reference profiles of density, thermal expansivity, and thermal conductivity of modelled mantle materials are given in Figure S3.

where η_0 is the reference viscosity at zero pressure and reference temperature T_0 (= 1600 K), E_a and V_a are the activation energy and volume, respectively, T is the absolute temperature, P the pressure, and R is the gas constant (8.314 J·mol^{-1} K^{-1}). Composition-dependency is considered through prefactor λ_c: a viscosity increase of one order of magnitude is imposed along the 660-km depth boundary (consistent with e.g., Čížková et al.,), and a viscosity decrease of 10^{-3} relative to the lower mantle is imposed at post-perovskite phase transition in the lowermost mantle (as suggested by Ammann et al.,). By considering a Newtonian rheology, the implicit dominant deformation mechanism is diffusion creep. Note, however, that we consider an activation energy that is smaller than experimental constraints for the upper mantle, an approach that can account for the effects of dislocation creep (e.g., Christensen & Hofmann, ,). With our chosen activation energy and volume, the activation enthalpy in the lower mantle varies from 262 kJ/mol to 548 kJ/mol, in line with perovskite predictions (Yamazaki & Karato,). An additional strain-dependency of viscosity is implemented through the weakening factor f_w (see next section). All physical and rheological parameters used in this study are listed in Table 2.

In order to obtain plate-like behavior at the surface, we assume that the material deforms plastically when a critical pressure-dependent yield stress is reached (as in Tackley, ,) (see Table 2). Plate-like behavior is evaluated using diagnostic criteria from (Tackley,): plateness p (the degree to which surface deformation is localized) and mobility m (the extent to which the lithosphere is able to move). An ideal plate tectonic style gives p = 1 and m close to or larger than 1.

2.4 Strain-dependent rheology

2.4.1 Finite strain

Our finite deformation approach follows that of (McKenzie,) and builds up on previous work (Xie & Tackley,). The deformation tensor M is tracked on the advecting tracers. At each timestep, the velocity gradient tensor is calculated and interpolated to the position of each tracer, from which the additional deformation for that timestep can be retrieved. This additional deformation is then added to the existing deformation tensor. A second-order accurate in time approach is implemented following (eqs. (7)-(10) in McKenzie,). This approach tracks stretching, rotation and advection in full tensor form (Fig. 2a). The eigenvectors of the matrix MM^T give the principal directions of the strain ellipse, and the square root of the eigenvalues of this matrix give the amount of strain in each direction (i.e., the semi-major and semi-minor axes a and b). This implementation has been tested and analysed in Supplementary Information Text S1. The scalar (finite) strain ϵ is calculated from the semi-major and semi-minor axes of the strain ellipse (see Text S2 for more detail) and is defined as:

$$\epsilon = log_{10}\left(\frac{a}{b}\right) \tag{2}$$

The deformation matrix M is reset to a unit matrix (i.e., the strain ellipse is reset to a circle) when a tracer undergoes melting-related differentiation or passes the depth of 660 km. This represents the resetting of the micro-structure of the rock when it melts or passes through the major 660 solid-solid phase transition (e.g., Solomatov & Reese,).

We have chosen to track deformation and apply weakening/healing (see below) in full tensor form, because this allows for analysis of full history-dependent deformation. This differs from other studies that only track the second invariant of strain rate (e.g., Tackley, ,). Tracking the deformation matrix (e.g. strain ellipse) also has many potentials for future research, including directional information of deformation related to mineral fabric, lattice-preferred orientation, and seismic anisotropy.

2.4.2 Strain weakening parametrization

Lower-mantle material is rheologically weakened following a simplified strain-dependent weakening curve (Fig. 2b):

$$f_{\mathrm{w}}(\epsilon) = 0.5 \cdot (1 + f_{\mathrm{w}}^{\max}) + 0.5 \cdot (f_{\mathrm{w}}^{\max} - 1) * \tanh\left[C \cdot (\epsilon_i - \epsilon_{\mathrm{crit}})\right] \tag{3}$$

where ϵ_{crit} is the critical strain threshold parameter (the strain at which half of the weakening has taken place, see Fig. 2b), $f_{\mathrm{w}}^{\max}$ is the maximum weakening factor (1 for no weakening), and C (= 2) controls shape of strain weakening curve. Eq. (3) was chosen as such to mimic a smoothly evolving weakening curve that can be easily parameterized (i.e., *tanh* function). Weakening occurs almost instantaneously as material becomes deformed (in agreement with Girard et al., , ,) and the general trend is in line with predictions from micro-scale numerical studies (with Thielmann et al., ,), see Text S2 for a more elaborated discussion. The maximum amount of weakening ($f_{\mathrm{w}}^{\max}$) is a free parameter. For simplicity, we neglect the composition-dependency of strain weakening, as well as the anisotropy of viscosity according to the strain tensor, to establish the first-order effects of strain-weakening rheology on the lower mantle. Neglecting anisotropy assumes that the strain ellipse is well-aligned with the dominant shear direction at any finite strain.

2.4.3 Rheological healing

Processes such as diffusion-dominated annealing and/or grain growth may lead to the relaxation of deformed grains (e.g. Solomatov & Reese,). For part of the models, we approximate such rheological healing by relaxing the deformation matrix (strain ellipse) towards a unit matrix (circle) with a temperature-dependent (grain growth highly

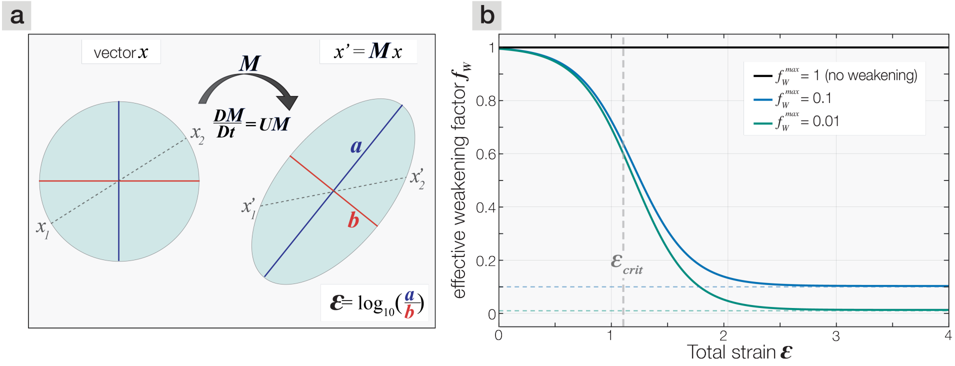

Figure 2. **(a)** The deformation matrix M relates a vector x connecting two nearby points at time t to the same vector at time zero. The time evolution of M on each tracer can be described by multiplying the velocity gradient tensor U with M (for details, see McKenzie,), and M is updated at each timestep on each tracer. **(b)** Weakening curve applied to all lower mantle materials in the models that explore the effect of strain-dependent rheology in the lower mantle on mantle dynamics (see Section 2.4.3, eq. 3). Input variables are $f_{\mathrm{w}}^{\max}$ (the maximum weakening factor f_{w}), the critical strain threshold ϵ_{th} (the strain at which half of the maximum weakening has taken place after which weakening occurs), and the shape factor C. A comparison of these weakening curves with other studies is presented in Figure S4b and discussed in Text S2.

depends on temperature) and pressure-dependent (diffusion is limited at higher pressures) term. This term may represent diffusion creep-dominated healing of micro-structures. Healing lowers the local strain ϵ and subsequently reduces the effective weakening. The temperature-dependency of rheological healing allows for long-term memory of deformation at cold temperatures and faster healing at deep mantle temperatures, whereas the pressure-dependency may counteract fast rheological healing at high T-P regions. Rheological healing is implemented as:

$$\frac{dM}{dt} = -H \cdot (M - I) \tag{4}$$

where H is the rheological healing rate ($H{=}\frac{1}{\tau_{\mathrm{h}}}$ with reference timescale of rheological healing τ_{h}). By rewriting eq. (4), M is updated as follows:

$$\frac{1}{M - I} dM = -H \cdot dt \tag{5}$$

$$\int_{M_{\mathrm{old}}}^{M_{\mathrm{new}}} \frac{1}{M - I} dM = \int_{t_{\mathrm{old}}}^{t_{\mathrm{new}}} -H \cdot dt \tag{6}$$

$$ln\left(\frac{M_{\mathrm{new}} - I}{M_{\mathrm{old}} - I}\right) = -H \cdot (t_{\mathrm{new}} - t_{\mathrm{old}}) \tag{7}$$

$$M_{\mathrm{new}} = M_{\mathrm{old}} \cdot exp\left(-H \cdot \Delta t\right) + I \cdot \left[1 - exp\left(-H \cdot \Delta t\right)\right] \tag{8}$$

where M_{new} is the updated deformation matrix, M_{old} is the deformation matrix before healing, Δt is the timestep in seconds ($= t_{\mathrm{new}} - t_{\mathrm{old}}$), and I is the unit matrix. This healing rate causes M to relax towards a unit matrix I. This relaxation produces a slight rotation of the strain ellipse, but this does not affect our model results since we assume isotropic properties. Text S1 shows a more detailed analysis of this healing implementation and an outlook on how to keep the orientation equal. The rheological healing rate H is temperature- and pressure-dependent following:

$$H(T, P) = H_{660} \cdot exp\left\{-\left[\frac{E_{\mathrm{a}} + (P - P_{660}) \cdot V_{\mathrm{a}}}{R \cdot T} - \frac{E_{\mathrm{a}}}{R \cdot T_{660}}\right]\right\} \tag{9}$$

where H_{660} is the reference healing rate (s^{-1}) at the top of the lower mantle ($P = P_{660}$, $T = T_{660}$, along the reference adiabat); this depth is chosen because weakening and healing only occur in the lower mantle. The activation energy and volume are assumed to be the same as those for diffusion creep because atomic (vacancy-) diffusion is the mechanism by which healing occurs. More information on this rheological healing rate, the chosen reference values, and how this parametrization ultimately affects the distribution of strain in the models is described in Text S3.

2.5 Automated detection of mantle domains

We use the geodynamic diagnostics toolbox StagLab (Crameri,) to automatically detect regional flows that are either self-driven (i.e., active) or induced (i.e., passive). Active regional flows represent mantle plumes (active upwellings) or active slabs (active downwellings). Passive slab remnants in the mantle that are not actively sinking, are not detected. Detecting mantle plumes using a purely thermal definition (e.g., Labrosse,) or a purely dynamic definition (e.g., Hassan et al.,) does not work for our set of numerical models, as our modelled plumes significantly vary in terms of their anomalies in both temperature and radial velocity. We use a new combined thermo-dynamical approach of identifying mantle plumes and slabs. As a summary, active plumes and slabs are defined based ona combination of the horizontal residual fields of temperature and radial velocity: $T_{\mathrm{res}} \cdot |v_{\mathrm{r,res}}|$. The residual fields T_{res} and $T_{\mathrm{res}} \cdot |v_{\mathrm{r,res}}|$ at each timestep are statistically analysed, and their percentiles are used for the definition of the plume/slab thresholds. More details on this approach is given in Text S4. Finally, the mantle diagnostics routine also detects thermochemical piles present atop the CMB based on composition and temperature. In terms of composition, pile material must consist of at least 60% of the pile must consist of basaltic material ($C_{\mathrm{bs}} \geq 0.6$), while the temperature constraint is defined using the average of a mid-mantle temperature of 3000 K and the CMB temperature: $T \geq (3000 + T_{\mathrm{CMB}}/2)$ [K] (as in Schierjott et al.,). Using this routine, the physical properties within all different mantle domains can be separately explored.

2.6 Parameter study

In this numerical study, we vary several parameters. Most of them are related to the newly-implemented strain-weakening parameterization: we systematically vary the maximum strain weakening factor $f_{\mathrm{w}}^{\mathrm{max}}$ from 1 (no weakening) to 0.01. The range of explored weakening factor (1-0.01) implies a viscosity contrast range of 1-100 between the "interconnected weak layers" (IWL) and "load-bearing framework" (LBF) viscosity mechanisms. For a ∼pyrolitic mantle, this would coincide with a viscosity contrast between bridgmanite and ferropericlase ranging from 1 to ∼200-300, which is consistent with mineral physics estimates (e.g. Yamazaki & Karato, ,). The reference healing rate H_{660} is varied in the range of 10^{-14}-10^{-16} s^{-1}, which corresponds to $\frac{1}{e}$ healing time scales of 3-300 Myr for the uppermost lower mantle. The fastest healing time of 3 Myr is in line with studies on single-mineral chemical diffusivity (using e.g. diffusivities of 10^{-18} m^2s^{-1} and $d = 1$ cm in (Ammann et al.,)). We expect such self-diffusion timescales to give lower bounds in terms of healing timescales for a complete mineral fabric. Finally, since these models including SW rheology show different final viscosity profiles, we select certain SW cases which we run again with an increased viscosity contrast between the upper and lower mantle ($\lambda_{660} > 10$). The combined effect of such increased intrinsic lower-mantle viscosity and strain weakening behavior (lowering the lower mantle viscosity) gives more similar final viscosity profiles. As such, the effect of a changing Rayleigh number on mantle dynamics is eliminated and the direct effect of SW rheology can be determined.

3 Results

The relevant model parameters and output variables of all models run in this study are summarized in Tables S1 and S2 (Supporting Information). Videos related to the cases discussed in the text and/or figures can be found in the Supporting Information related to this article. All models show plate-like behavior according to the diagnostics of (Tackley,), and final average viscosity profiles of most models approximately agree with estimates from literature (see Figure S4). We first describe the evolution of our reference model (Section 3.1). In this model, the strain field is tracked according to the newly-implemented finite strain approach without the application of strain-dependent weakening or rheological healing. In Section (3.2), we describe the effect of the implemented strain-weakening rheology on model behavior. Two case studies are highlighted with various degrees of strain-weakening and rheological healing. Finally, in Section 3.3, we summarize the results of several case studies with various degrees of SW, but a similar final viscosity profile (Section 3.3).

3.1 Reference model evolution

The temporal evolution of our reference model (M_0), which does not include strain-weakening, is shown in Fig. 3 and Video S1. Soon after the model onset, the thermal boundary layers grow in amplitude, and after ample growth of boundary layer instabilities, a mantle overturn initiates the onset of whole-mantle convection and plate-tectonic behavior (Table S1). The viscous flow associated with early model dynamics (at 1.0 Gyr) causes a lower-mantle strain field that is localized in regions of buoyant, hot upwellings, and areas which are deflected by incoming, strong lithospheric drips/slabs (Fig. 3a). From the start of whole-mantle convection, the mantle gradually cools and the frequent occurrence of active mantle plumes and subducting slabs and active mantle plumes causes further complexity of the mantle strain pattern (Fig. 3). As the deformation history is reset at the 660 km boundary layer, small-scale strain patterns in the upper mantle are

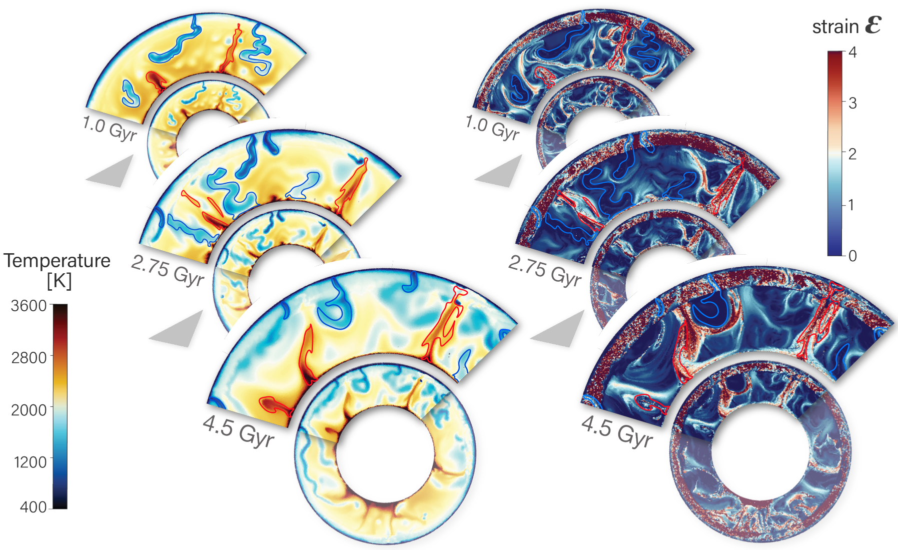

Figure 3. Temporal evolution of the reference model M_0, in which neither rheological healing nor rheological weakening is applied. Three snapshots of the temperature field (left) and strain field (right) are shown. Red outlines the edges of detected mantle plumes, and blue that of active downwellings (see Section 2.5 for their definitions).

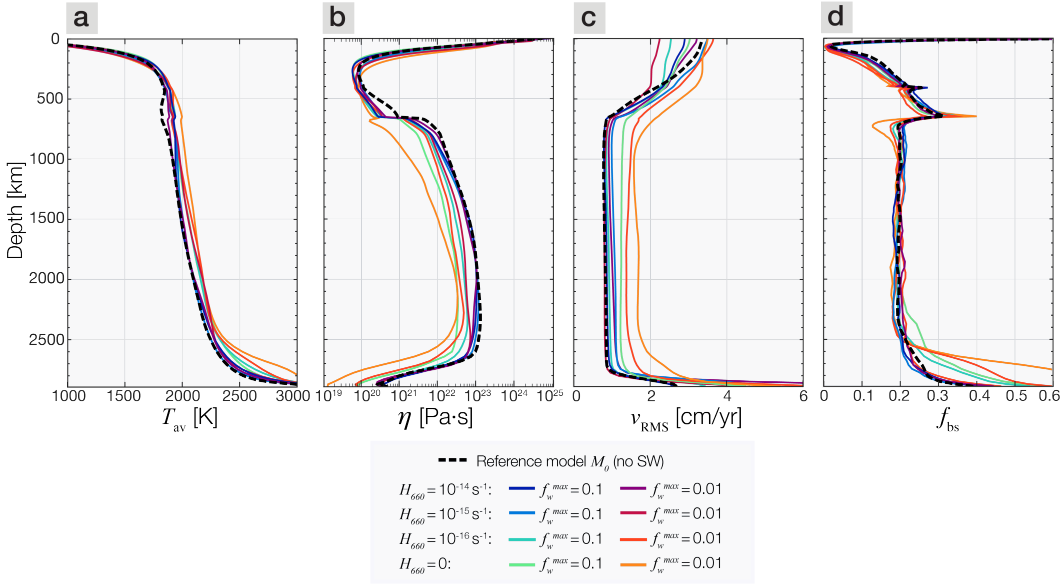

Figure 4. Radially averaged profiles of **(a)** temperature T, **(b)** viscosity η, **(c)** RMS velocity v_{RMS}, and **(d)** basalt fraction f_{bs} for all main models in this study. All radial profiles are averaged over time between 4.0 and 5.0 Gyr model time.

not carried into the lower mantle. Instead, strain builds up in downwelling (e.g., around slabs) and upwelling regions (plumes) of the lower mantle (Fig. 3).

The radially-averaged temperature profile displays the typical signal of efficient whole-mantle convection with boundary layers superimposed on a mostly adiabatic geotherm (Fig. 4a). The radial viscosity profile reflects the temperature- and depth-dependent rheology, as well as its compositional dependency expressed as a viscosity step towards higher values from the upper- to lower mantle (λ_{660}) (Fig. 4b). Mantle velocity is highest in the bottom ~150 km of the lower mantle and in the upper mantle (Fig. 4c). Finally, the compositional profile shows efficient basalt segregation in a thin region on top of the CMB and in the mantle-transition zone (Fig. 4d).

3.2 Influence of strain-dependent rheology

In this section, we separately describe the effects of SW rheology on several key aspects of mantle convection which were introduced in Section 1. First, the effect of SW rheology on convective flow patterns is described (Section 3.2.1), followed by its effect on the thermal evolution of the mantle (Section 3.2.2), on thermochemical piles formation (Section 3.2.3), and on the dynamics of mantle plumes (Section 3.2.4).

3.2.1 Global mantle convective patterns

The radial profiles of viscosity and root mean-square (RMS) velocity of modelled mantles (Fig. 4b-c), as well as their final averages (Fig. 5b-c) show clear trends for SW rheology models. The average mantle viscosity is significantly lowered when SW rheology is applied, mostly in the lower mantle (Fig. 4b). Final convective vigor ($\sim v_{\mathrm{RMS}}$) is increased for most SW models, also mainly accommodated in the lower(most) mantle (Fig. 4c). Figure 6 shows the detected mantle domain field, i.e., passive/active up - and downwellings, of three selected models with variable degrees of SW rheology at ~4.5 Gyr. It further shows the temporal evolution of the lateral distribution of this mantle

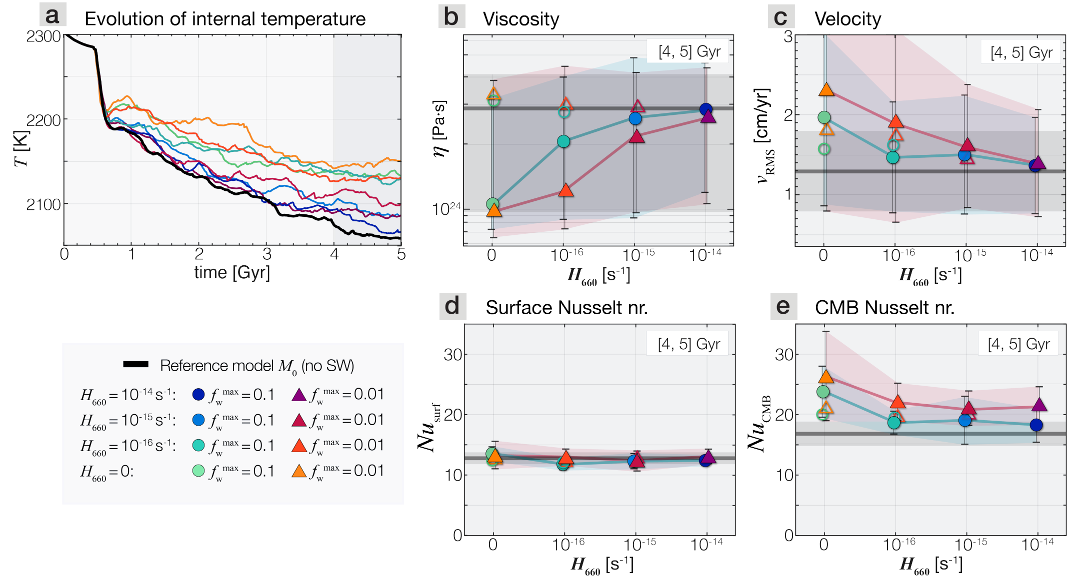

Figure 5. **(a)** Evolution of internal temperature for all main models, colors represent reference healing rate and applied weakening factor (see legend). **(b)-(e)** Selected output parameters (viscosity, velocity, surface and bottom Nu number) averaged between 4.0 and 5.0 Gyr of model time. The black line represents the reference model (neither strain-weakening nor rheological healing), with the gray shaded area showing the standard deviation. The horizontal axis represents the reference healing rate H_{660}, and the icon shape stands for the implemented strain-weakening factor $f_{\mathrm{w}}^{\max}$. The error bars and colored shaded areas indicate the standard-deviation of the parameter over that time period. For selected cases, outline-only symbols are also plotted, which represent the results for the additional cases with an increased viscosity jump at the 660 km discontinuity (see Section 3.3).

domain field at 1800 km depth (i.e., in the middle of the lower mantle). In comparison to the reference model (Fig. 6a), SW models with an increased convective vigor show a more chaotic planform of mantle flow (Fig. 6b,c) with a larger number of small plumes present. The timescale of convection decreases with SW rheology as the convective vigor increases (overturn time $\tau \sim \frac{1}{v_{\mathrm{RMS}}}$, Miyagoshi et al. ()). The length-scale of convection also decreases with SW rheology as the lower mantle consists of convection cells with smaller aspect ratios, i.e., more narrow regions of up- and downwellings (Fig. 6b,c). The temporal evolution shows that the upwelling plumes in the lower mantle have shorter lifetimes than those in non-SW models. Figure 7a-c show the distribution of selected quantities in the whole mantle domain for the same three models. The v_{RMS} histograms for SW models are more skewed than that for the reference model, highlighting small domains in the mantle with very high velocities. This highlights the (albeit small) domains in which SW efficiently occurs. Interestingly, despite the changing pattern and vigor of mantle flow (described above), the statistical distribution of the age of mantle materials (defined by the time since a tracer last underwent a melting episode) in the whole mantle is similar for cases with and without SW (right panels of Fig. 7).

3.2.2 Thermal evolution

In models with SW rheology, the mantle cools down to higher final equilibrium mantle temperatures than in models with less or no SW rheology (Figs. 5a and 4c). Even

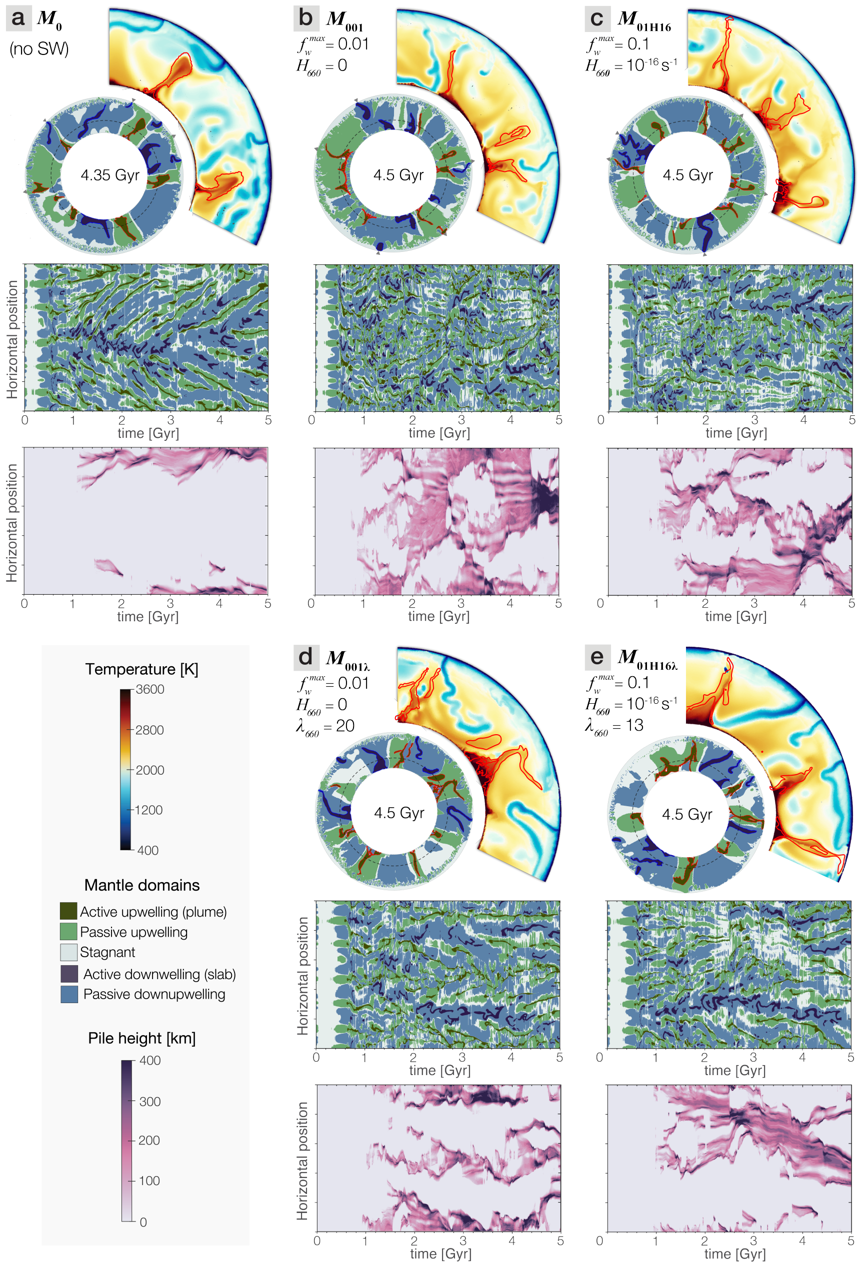

Figure 6. Top: age-of-the-Earth snapshots for five selected models showing the mantle domain field and a zoom-in of the temperature field. Middle: temporal evolution of the lateral distribution of this field at 1800 km depth. Red outline: active mantle upwellings, blue outline: active mantle downwellings. See Section 2.5 for the definitions of the mantle domains. Bottom: temporal evolution of the lateral distribution of detected thermochemical piles atop the core-mantle boundary, color-coded according to the height of the detected pile. **(a)** Reference model: neither SW rheology nor rheological healing, **(b)** extreme case of strong strain-weakening and no rheological healing, and **(c)** model with SW rheology and healing simultaneously activated. **(d)** Additional case, same as (b) but with an increased viscosity jump at the 660 boundary (λ_{660}). **(e)** Additional case, same as (c) but with a higher λ_{660}. See Section 3.3 for description of (d)-(e).

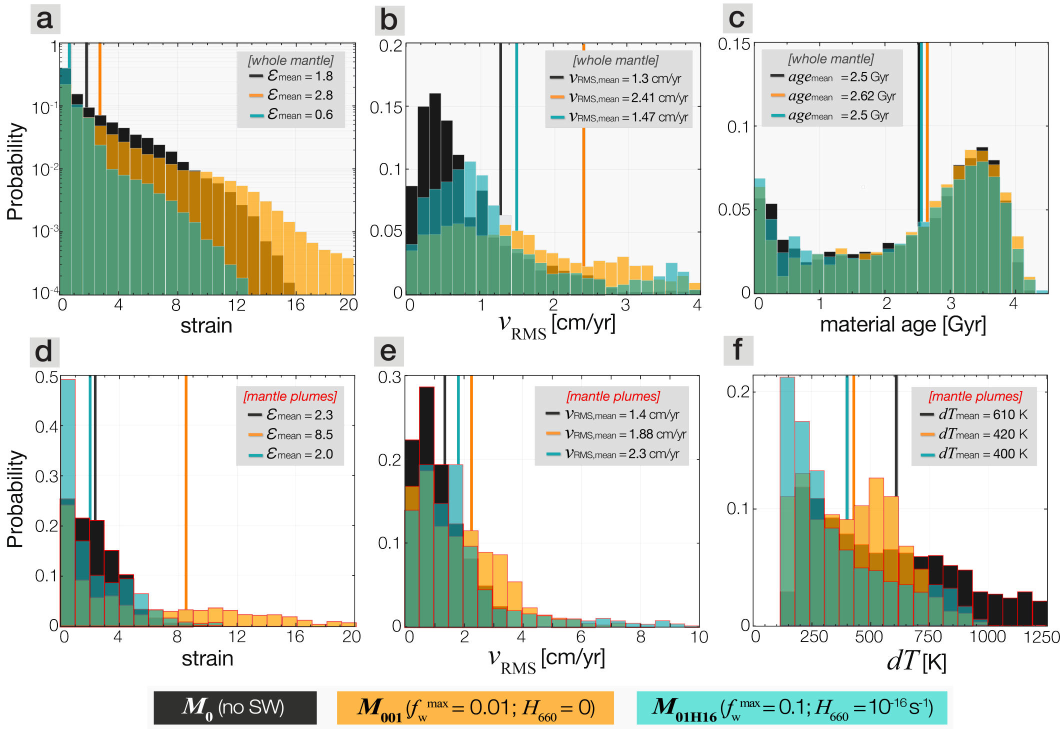

Figure 7. Histograms of selected quantities for selected models (color scale), averaged between 4.0 and 5.0 Gyr of model time. **(a)-(c)** show the distribution of the strain field (ε), the root mean-square velocity (v_{RMS}), and the material age (age) within the whole mantle domain. **(d)-(f)** show the distribution of the strain field (ε), the root mean-square velocity (v_{RMS}), and the average horizontal temperature anomaly of the material (dT) within the detected active mantle upwellings (plumes). The vertical lines represent the mean values for each histogram. Note the vertical axis of the strain histogram in panel **(a)** is logarithmic, whereas that in **(d)** is not.

with a high healing rate of $H_{660} = 10^{-14}$ s^{-1}, which causes strain in the lower mantle to heal on short geological timescales (Text S3), higher final internal temperatures are reached. This is also apparent by the relation between top and bottom Nusselt number (Nu_{top} and Nu_{bot}). Nu_{top} is not much affected by strain-weakening rheology, while Nu_{bot} is on average significantly higher for SW models (Fig. 5d). Likely, Nu_{top} is not much affected since convective stresses at the base of the lithosphere are roughly similar for all cases due to similar upper-mantle viscosities (see Fig. 4b). A higher Nu_{bot} implies that heat is more efficiently removed from the core. In our models (constant core temperature), this causes a higher final mantle temperature in models in which SW rheology is applied. How our assumption of constant core temperature may affect these results is discussed in Section 4.4.

3.2.3 Formation of piles

Basalt segregation is most efficient in models with strong SW, because these models exhibit a low-viscosity, high-temperature mantle (see above and Figs. 4d, and Videos). Due to efficient segregation in these models, basaltic material tends to settle more efficiently in the lowermost mantle, stabilizing the formation of large thermochemical piles that cover more of the CMB (Fig. 6; Table S1). Also, the transition zone (410-660 km depth) becomes more enhanced in basaltic material ($f_{\mathrm{bs}} \approx 40\%$), while the regions around it are more depleted (Figs. 4d) (as in e.g. Ogawa, , , ,). Moreover, the thermochemical piles are internally convecting in SW models, affecting overall heat fluxes through the mantle: due to the high intrinsic pile density, heat can build up within the piles, forming another thermal boundary layer on top of them. Thus, these piles can act as plume generation zones in the models as active upwellings sporadically form on top of them, as well as along their edges.

3.2.4 Plume dynamics

Strain mainly localizes in hot upwellings, where material is deformed soon after model onset and subsequently subjected to weakening. Even in the presence of rheological healing, plume channels are still weakened due to strain localisation (see Supporting Information Text S3 and Fig. S3). According to classical thermal plume formation theories (e.g., Howard,), the temperature and width of a mantle plume is related to the time over which the boundary layer grows. A thermal instability occurs when the critical boundary layer Rayleigh number is reached ($Ra_{\mathrm{local}} = Ra_{\mathrm{local,crit}}$) (Howard,). If the viscosity of the material is large (low Ra_{local}), longer onset times occur, i.e., the growth rate of the instability depends inversely on the local viscosity (e.g., Howard, , ,). In our SW models, the lower viscosity of weakened plume materials would, according to the theory above, decrease the onset times of the instabilities. In these SW thermal instabilities, there would is also a smaller temperature build-up compared to non-SW thermal instabilities. This precludes the growth of a wider, anomalously hot mantle plume with mushroom-shaped heads as seen in our reference model (Fig. 6a). This absence of mushroom-shaped plume heads is evident for weakened plumes in both pure SW cases as well as SW + rheological healing models (Fig. 6b-c and Videos S2-S3).

The positive feedback between weakening and strain localization causes a low-viscosity channel to form in and around plumes, allowing for rapid transport of mass and heat from depth towards the surface. The typical velocities in the plume conduit increase for more efficient SW (i.e., for lower $f_{\mathrm{w}}^{\mathrm{max}}$ or lower H_{660}), while the excess temperatures are lower for more efficient SW (Fig. 7, Table S2). These distinct plume dynamics caused by SW rheology are further apparent in the bottom Nusselt number (Nu_{bot}). Final Nu_{bot} is, on average, higher for models with most efficient SW rheology, linked to the thinner thermal boundary layers and higher boundary layer Rayleigh numbers (Fig. 5f). This prediction implies that heat is more effectively lost by convection (i.e., via mantle plumes) rather than conduction. The weakened conduits are easily deflected by background flow or by incoming slabs (see Videos S2 and S3). Typical timescales of plume lifetimes decrease from 500$\sim$ 1000 Myr for the reference case to few 100 Myrs for the extreme SW cases (lower panels in Fig. 6).

3.3 Influence of the mantle viscosity profile

Each model discussed above displays a distinct effective viscosity profile through time (Fig. 4), which, in turn, controls convective vigor and thereby strongly affects model evolution. In order to distinguish the direct (first-order) effects of SW rheology on mantle dynamics from the indirect effects of SW rheology through the radial viscosity profile (second-order), we explore five additional SW cases with a higher intrinsic viscosity jump at 660 km depth (λ_{660}), such that the final viscosity profile is similar to that of the reference case M_0, and to each other (see Fig. 8b). Videos S4 and S5 show the time evolution of internal dynamics for two selected cases (those illustrated in Figures 6d-e and 9).

These additional cases show a similar average thermal evolution as the reference case (Fig. 8a). Despite the similarities in mantle viscosity, the convective vigour is still affected by SW due to localization of flow. The average values for v_{RMS} are $\sim$50% higher in the additional SW models than in the reference model case (Table S2; Fig. 9b). In

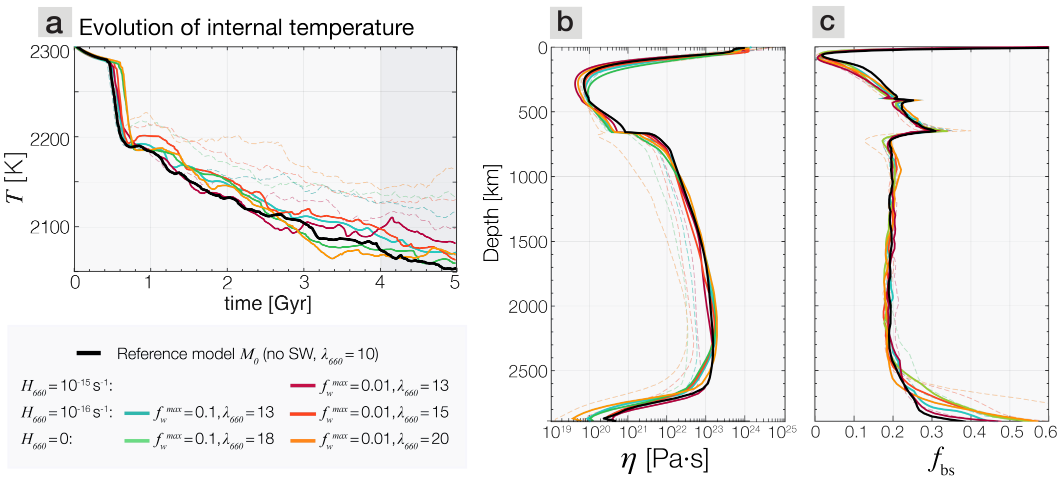

Figure 8. **a)** Temporal evolution of internal temperature for reference model case (black line) and additional SW cases (color-coded) with variable weakening + healing scenarios and an increased lower mantle viscosity jump. **(b)** All of these cases display a similar final lower mantle viscosity profile. **(c)** Basalt radial profiles. The radial profiles are averaged between 4 and 5 Gyr. The dashed lines are the SW models corresponding to the additional cases but with λ_{660}=10.

particular, the v_{RMS} histogram is more skewed, with high values (> 2 cm/yr) for SW models, and hardly any such very high velocity domains for the reference case (Fig. 9b). Most of this faster flow is focused in narrow, weakened upwelling regions (Fig. 9b,e and Videos S4-S5). The higher convective vigor, in turn, affects the pattern of mantle flow (Fig. 6d-e), but much less so than the corresponding SW rheology models with a fixed $\lambda_{660} = 10$ (Fig. 6b-c). Despite more similarity of the length- and timescales of convection for the additional SW cases and the reference case, SW rheology still causes the formation of narrower convection cells and more mantle plumes with shorter lifetimes (Fig. 9b-c). In terms of the distribution of the age of all mantle materials (Fig. 9c), the mean age is indistinguishable between cases. Further, top Nusselt numbers are similar between cases. In turn, bottom Nusselt numbers are still slightly increased in the additional SW rheology models (Fig. 5d-e), but much less than in the related SW rheology models with a fixed $\lambda_{660} = 10$. These results strengthen our conclusion that CMB heat flux is preferentially accommodated via convection vs. conduction, particularly in models with SW. However, plume dynamics and the size of thermochemical piles are still affected in the same way as in the previously described SW models. In fact, the localization of increased flow velocity in the narrow upwelling mantle plumes is even significantly more pronounced in these additional SW models. Moreover, thermochemical piles in the additional SW models are still substantially larger. Hence, we conclude that SW rheology is the critical ingredient for the weakening of plume channels, their narrow shapes and relatively low thermal anomalies, as well as the formation and stabilization of large thermochemical piles. Second-order effects, such as the higher final mantle temperature, and the significantly higher average mantle flow velocities, are caused by the modification of the viscosity profile through SW.

Based on the outcomes above, we conclude that SW rheology is the critical ingredient for (i) weak and (ii) narrow plumes with (iii) relatively low thermal anomalies, as well as (iv) large and long-lived thermochemical piles. Secondary effects of SW rheology, such as on CMB heat flux and mantle cooling, are caused by its effects on mantle dynamics by increasing convective vigor (locally). At a fixed average lower-mantle vis-

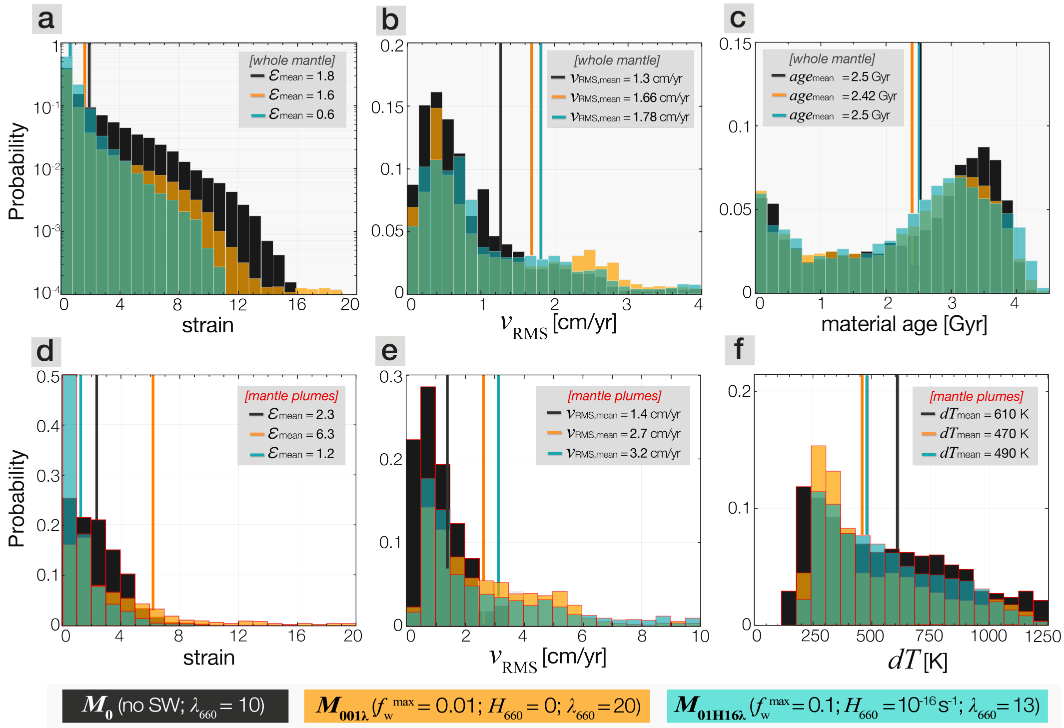

Figure 9. Histograms of selected quantities for the reference model M_0 (black) and two additional cases with variable combinations of strain-weakening and healing plus an increased viscosity jump (λ_{660}) at the 660 km discontinuity (orange, blue). The colour scheme corresponds to that in Figure 6, with the difference being the higher viscosity jump in the additional cases explored here. See Section 3.3 for details. **(a-c)** Distribution of the strain field, the root mean-square velocity, and the material age within the whole mantle domain. **(d-f)** Distribution of the strain field, the root mean-square velocity, and the average horizontal temperature anomaly of the material within the detected active mantle upwellings (plumes). The vertical lines represent the mean values for each histogram.

cosity, CMB heat flux and mantle thermal evolution is still affected by SW, but much less so than in the models discussed in Section 3.2.

4 Discussion

4.1 Mantle mixing and geochemical reservoirs

With an increasing convective vigor and decreasing length-scale of convection for SW models (Fig. 6), one might expect mixing efficiency of mantle material to increase (e.g., Coltice & Schmalzl,). However, in high convective-vigor SW models, basalt more easily segregates from harzburgite and thermochemical piles, which are in turn more stable over time (Section 3.2.3). Such a relation between lower mantle viscosity and more efficient basalt segregation is consistent with other studies (e.g., Yan et al.,). Hence, heterogeneity mixing turns out to be less efficient in models with SW rheology. Yet, the statistical distribution of mantle material age in the whole mantle is similar for all cases (Figs. 7c and 9c). While a slightly higher proportion of very ancient material (>4 Ga) is preserved in SW models, a significant part of this material portion is accommodated in the larger thermochemical piles. The similarity of preservation in all our models, and particularly in the convecting mantle, is contrary to earlier suggestions that SW promotes the survival of primordial materials (e.g., Girard et al., ,). In our SW models, convection patterns are not critically stabilized over time. This result may be attributed to the lack of effective strain weakening in the low-strain downwelling regions. Only if both upwellings and downwellings were significantly weaker than the regions in-between, efficient preservation may occur in these in-between regions (Ballmer et al., ,). For example, it has been proposed that grain-size reduction in cold slabs that enter the lower mantle causes local weakening (Ito & Sato, , , ,). Such grain-reduction weakening in combination with SW plumes may cause a style of convection dynamics more akin to previously proposed (Fig. 1b), with weakening occurring in both downwelling slabs and upwelling plumes. Future work should test if this is indeed the case.

4.2 Planetary interior evolution

Since SW rheology in the lower mantle affects CMB heat fluxes and their ratio to surface heat fluxes (Fig. 5, Table S1), it may have a substantial control on core dynamics as well as mantle cooling rates. The heat transfer from the core into the base of the mantle greatly affects the sustainability of a planetary dynamo through its control on the vigor of core convection, and the onset time of inner core crystallization (Stevenson, ,). Moreover, the spatial pattern of (geo-)magnetic secular variations is commonly attributed to changes in CMB heat fluxes and mantle plumes (e.g., Larson & Olson, , ,).

Modern estimates of CMB heat flux for the Earth range from several TW up to 15 TW (e.g., Lay et al., , ,), i.e., significantly lower than outcomes in our numerical models (Table S1). However, these estimates may be underestimated since they do not consider additional CMB heat flux by advection due to cool plumes (subducted slabs) arriving at the base of the mantle (Labrosse,). In turn, our models neglect internal heating (as they are not tuned to exactly match Earth thermal evolution), and thus overestimate plume activity and strength (e.g. Mckenzie et al.,). They also ignore core cooling (constant core temperature of 4000 K), and hence early and present-day CMB heat fluxes are likely underestimated and overestimated (Labrosse,), respectively. Nevertheless, in our models, mantles with SW rheology pull out heat more efficiently from the core, which would alter planetary thermal evolution. If core cooling were combined with SW rheology, the core would likely tend to cool faster which, in turn, would lower CMB heat flux and possibly final mantle temperatures. At a given present-day geotherm, this may imply hotter early-core and early-mantle temperatures, and/or more early mantle melting. Future studies should investigate the combined effect of SW rheology and core cooling, and assess whether the indirect effect of SW on mantle temperatures (i.e., only minor when comparing models with similar viscosity structures, see Section 3.3) still holds.

The relevance of SW rheology for (exo-)planets depends on their mineralogy and internal structure. Stars in the solar neighborhood show diverse Mg-Fe-Si compositions (Hinkel et al.,). Assuming stellar compositions as a proxy for rocky planet compositions (as in Spaargaren et al.,), planets in stellar systems with Mg/Si$<$1 likely have no ferropericlase in their mantle, hence no strain weakening is expected to occur. Rocky planets associated with Mg/Si$\gg$1.5 stars feature significant amounts of ferropericlase in their mantles, hence mantle rocks would form a IWL at very small (or even zero) strain. The majority of rocky exoplanets should have an Earth-like bulk composition with 1$<$Mg/Si$\ll$1.5 (e.g., Putirka & Rarick, ,), where SW rheology potentially occurs in the mantle. Moreover, a recent study established the stability of a very weak B2-(Mg,Fe)O phase under extreme pressures (Coppari et al.,), which may dramatically affect the deep-mantle rheology of Super Earths.

4.3 Thermochemical piles

The current degree-2 pattern of Earth's mantle flow, anchored by the two antipodal LLSVP piles (Dziewonski et al.,), has been suggested to be a stable energy configuration from the point of view of Earth's moment of inertia and to exist for at least 200 Myrs (Burke et al., , , ,). Yet, this configuration is only energetically stable if LLSVPs are (much) denser than slabs, which remains unclear (Koelemeijer et al., , ,). The intrinsic high density of recycled crustal materials (basalt) causes piles to form in our models (Fig. 6), in agreement with various geodynamical studies (Nakagawa & Buffett, , , ,). Here, we show how SW rheology causes more efficient basalt segregation, and the formation of piles that cover a larger extend of the CMB (see Fig. 6 and Table S1). Such thermochemical piles can act as a thermal insulator of part of the heat coming from the CMB (e.g., Lay et al., ,). Yet, the overall CMB heat flux is increased in SW rheology models. These increased values are accommodated by the much larger fluxes within the weakened plume channels (Supporting Information Table S2) as well as small-scale convective fluxes within the piles (e.g., Fig. 6b). Plumes formed from this (secondary) thermal boundary layer have by default less heat available (Farnetani,), since the temperature difference between the piles and ambient mantle is less than that between the adiabat and the CMB. This could partially explain lower temperature anomalies of these mantle plumes, although note that weakened plumes not only rise from the piles, but also from the CMB (see Figs. 6, S6, and Videos S2-S5).

4.4 Plume formation

As described in the Section 3.2.4, the differences in plume dynamics between our numerical models agree well with scalings and relationships found in early classical thermal plume formation theories (e.g., Howard, , ,). In our models, plumes weakened by SW rheology differ most from the classical head-and-tail plume structure (Richards et al., , , ,) . Weakening of narrow conduit provides a pathway (lubrication channel) through which hot material can readily rise. In such weakened plume conduits, transport of mass and heat occurs more efficiently. As relatively little thermal buoyancy needs to be built up to drive the plume, no head-and-tail geometry is formed. Indeed, a number of studies have shown that the conduit radius is proportional to $\eta^{1/4}$, where η is the viscosity of the hot thermal boundary layer (Griffiths & Campbell, ,). Such narrow weakened plume conduits have a shorter lifetime than non-weakened plumes (Fig. 6) and can be more easily diverted by large-scale mantle flow and rheological contrasts in the mantle, as is visualized in the supplementary Videos. An alternative mechanism for the generation of non-classical (e.g., head-less) plumes is the entrainment of intrinsically dense materials. Thermochemical plumes have been found to display highly variable shapes and ascent styles, and to be generally wider than thermal plumes (Farnetani & Samuel, , ,).

Most, if not all plumes in our models are also of thermochemical origin (i.e., due to the entrainment of basalt), with negligible compositional differences between SW and non-SW models (see Table S2). However, the entrained basalt fractions are rather small ($f_{\mathrm{bs}} \sim 0.25$), and hence the effects of strain weakening on plume ascent geometry are dominant. At a reference depth of 1800 km, the basalt fractions in our SW and non-SW models correspond to average plume buoyancy numbers B_{pl} (as formulated in e.g. Davaille, ,) of 0.1-0.21, see Table S2. Such low B values indicate that thermochemical effects alone cannot account for variable plume shapes, particularly as basalt fraction for SW and non-SW models are similar.

4.5 Mantle plumes on Earth

On Earth, the mismatch between lower mantle and core adiabats implies a super-adiabatic temperature jump across the CMB of about 1000-1500 K (Jeanloz & Morris, , ,). Most mantle plumes on Earth, however, are inferred to have excess temperatures of only 100-300 K (e.g., Albers & Christensen,). When extrapolating such excess temperatures to the lower mantle, temperature anomalies of about 500 K have been inferred at the CMB (Albers & Christensen,), still lower than the expected CMB temperature difference (Boehler,). It has been argued that this mismatch is an indication for the super-adiabatic ascent of plumes (Bunge,), or that plumes rise from the top of a compositionally distinct layer at the base of the mantle (Farnetani,). Strain-weakening rheology of lower mantle materials could additionally help to explain the discrepancy between expected thermal anomalies and observed thermal anomalies of deep-seated mantle plumes, via the shorter onset times of thermal instabilities (see Section 3.2.4). On Earth, many deep-rooted plumes are thought to ascend within a few tens of million years to the base of the lithosphere (e.g., Torsvik et al.,). From our modelled mantle plume upwelling velocities, predicted average ascent times are reduced from $\sim$200 Myr (for non-SW models) to an $\sim$110 Myr (with SW). The fastest plumes in our SW models have ascent times of only 30 Myr (for 8 cm/yr rising speed), in contrast to 70 Myr for the fastest non-weakened plumes. Therefore, SW rheology could help to explain the plume rise speeds in the Earth's mantle. An alternative explanation for fast plume ascent involves stress-dependent non-Newtonian rheology in the lower mantle (van Keken,), which is argued to produce significantly reduced plume ascent times - although in combination with larger temperature excesses (van Keken,), which is not the case for weakened plumes in this study. Moreover, recently, several surprisingly 'cool' hotspots have been identified on Earth (Bao et al.,), attributed to either a passive upwelling, shallow source, or entrainment and small-scale convection. We suggest that SW rheology may be a key ingredient for unconventional deep-sourced 'cool' mantle plumes as identified by Bao et al. ().

Even though LLSVPs have been commonly linked to plume generation (e.g., Torsvik et al.,), this link remains controversial. French and Romanowicz () used whole-mantle seismic imaging techniques to argue for the presence of broad, quasi-vertical plumes (i.e., $\sim$1000 km in width) beneath many prominent hotspots. These broad plumes were inferred to be thermochemical in origin and rooted at the base of the mantle in patches of greatly reduced shear velocity (e.g., LLSVPs). Other studies propose that the same seismic structures are actually a collection of poorly-resolved narrow mantle plumes (Schubert et al., , ,). In this scenario, LLSVPs are in fact a cluster of plumes rather than being made up of stable, wide thermochemical piles with broad plume structures atop (as argued by French & Romanowicz,). In our models, SW rheology promotes the existence of multiple weak and thin plume channels, that could possibly be imaged as plume clusters. Yet, in contrast to the plume bundle hypothesis (Schubert et al., ,), such narrow, weakened plumes occur in combination with stable, thermochemical piles in the lowermost mantle, and they rise mostly vertically throughout the mantle. It must be noted that even with state-of-the-art seismic methods, narrow mantle plumes (especially those weakened by SW) are difficult - even impossible - to be uniquely distinguished (e.g. Kumagai et al., ,); hence further methodological advances are needed to convincingly discriminate the effects of strain weakening. Moreover, time-dependency is a key factor when interpreting present-day tomographic images of mantle upwellings. The image of a conduit rising from the CMB all the way to the lithosphere is only valid during part of the plume's lifetime (Davaille & Vatteville,). Therefore, plumes might not be easy to detect in tomographic images, particularly if they are weakened by SW rheology and/or deflected by mantle flow. Due to the SW effect on plume width and lifetime, SW rheology could help to explain the faint seismically slow anomalies - or even the absence of detectable anomalies - beneath several hotspots, such as Louisville, Galapagos, and Easter (Davaille & Romanowicz,).

4.6 Future studies

Several future scientific avenues may be carried out to advance this study on the effect of SW rheology on mantle dynamics. First of all, future studies could advance our implementation by making the SW rheology composition-dependent, causing strain-dependent weakening to mainly occur in ferropericlase-enhanced regions. Subducted oceanic crust at lower mantle conditions does not contain any ferropericlase, but instead, contains much cubic $CaSiO_3$ perovskite (Hirose, Sinmyo, & Hernlund, , ,), which may be intrinsically weak (Immoor et al.,). It is further interesting to test this composition-dependent weakening in combination with the existence of ancient bridgmanite-enhanced regions in the mid-mantle (as in Gülcher et al., ,), which should not exhibit SW due to the absence of ferropericlase, hence promoting their preservation. Moreover, it remains to be explored how strain-dependent and grain size-dependent rheology interact with each other in the lower mantle (see Section 4.1). Finally, with the tracking of the deformation matrix in full tensor form, additional work can focus on the direction-dependency of the strain ellipse and weakening behavior and their effects on whole-mantle dynamics.

5 Conclusions

- We implemented a new strain-dependent rheology for lower mantle materials, combining rheological weakening and healing, in numerical models of global-scale mantle convection.
- Strain particularly focuses in anomalously hot regions, such as piles atop the CMB and hot mantle plumes, also when rheological healing is applied.
- SW rheology is the key ingredient for the weakening of plume channels as well as forming large thermochemical piles
- Second-order effects of SW rheology, caused by the changing mantle dynamics due to a reduction of viscosity in the lower mantle, are higher equilibrium mantle temperatures and the significantly higher average mantle flow velocities.
- Weakened mantle plumes form narrow lubrication channels in the mantle through which hot material readily rises, and they have shorter lifetimes.
- This new kind of plume dynamics may explain moderate plume excess temperatures beneath hotspots (only up to 200–300 K), given the much larger temperature difference across the core–mantle boundary ($\sim$1000 K).

Acronyms

Myr million year
Gyr billion year
LBF load-bearing framework
IWL interconnected weak layers
CMB core-mantle boundary
LLSVP large low shear-wave velocity province
SW strain-weakening

Open Research

The open-source StagLab toolbox (Crameri,) was used for detecting different mantle domains in the numerical models, creation of histogram data (Figs. 6-7, S6-S7), and creating the Videos S1-S5. The new mantle domain detection scheme (as discussed in Supporting Information Text S4) is implemented in a STAGLAB 6.0 version, and it is available on https://doi.org/10.5281/zenodo.6801104 (STAGLAB-OS release for SW paper (G-cubed, 2022), v1.0.0 DOI: 10.5281/zenodo.6801104). Moreover, the open-source Python module StagPy (https://stagpy.readthedocs.io/en/stable/, last access: 17 July 2021) was also used for post-processing of the numerical data and production of radial and temporal profiles (Figs. 4, 5, S2, S4, and S5). The numerical code is available by reasonable request to Paul J. Tackley. All the data corresponding to the Figures and Tables shown in this paper, as well as the input files for all model runs, are given on https://doi.org/10.5281/zenodo

(DOI: 10.5281/zenodo.6805415). As the raw data of the numerical experiments of this paper are too large to be placed online (several TB), they can be requested from the corresponding author (Anna J. P. Gülcher).

Supporting Information

1. Text S1 to S4
2. Figures S1 to S7
3. Tables S1 and S2
4. Videos S1 to S5

Acknowledgments

This research has mainly been supported by the ETH Zürich Research Commission (grant no. ETH-33 16-1). M. T. was supported by the Bayerisches Geoinstitut Visitor's Program. We thank Lukas Fuchs for helpful discussions related to this work, Fabio Crameri for discussions related to visualisations and colormaps, and Albert de Montserrat for sharing data from (de Montserrat et al.,) for Figure S4b. We thank Juliane Dannberg for constructive comments that helped to improve the manuscript considerably. All numerical simulations were performed on ETH Zürich's Euler cluster. For the figures showing 2D snapshots of the models, we used the open-source software ParaView (http://paraview.org, last access: 2 September 2021), and the supplementary videos were made using the geodynamics diagnostics toolbox StagLab (Crameri,). Several perceptually uniform scientific color maps (Crameri, 2018, https://doi.org/10.5281/zenodo.1243862) were used to prevent visual distortion of the figures.

References

Albers, M., Christensen, U. R. (1996). The excess temperature of plumes rising from the core-mantle boundary. *Geophysical Research Letters*, *23*(24), 3567–3570. doi: 10.1029/96GL03311

Ammann, M. W., Brodholt, J. P., Wookey, J., Dobson, D. P. (2010). First-principles constraints on diffusion in lower-mantle minerals and a weak D" layer. *Nature*, *465*(7297), 462–465. Retrieved from `http://dx.doi.org/10.1038/nature09052` doi: 10.1038/nature09052

Arnould, M., Coltice, N., Flament, N., Mallard, C. (2020). Plate tectonics and mantle controls on plume dynamics. *Earth and Planetary Science Letters*, *547*, 116439. Retrieved from `https://doi.org/10.1016/j.epsl.2020.116439` doi: 10.1016/j.epsl.2020.116439

Ballmer, M. D., Houser, C., Hernlund, J. W., Wentzcovitch, R. M., Hirose, K. (2017). Persistence of strong silica-enriched domains in the Earth's lower mantle. *Nature Geoscience*, *10*(3), 236–240. doi: 10.1038/ngeo2898

Bao, X., Lithgow-Bertelloni, C. R., Jackson, M. G., Romanowicz, B. (2022). On the relative temperatures of Earth's volcanic hotspots and mid-ocean ridges. *Science*, *375*(6576), 57–61. doi: 10.1126/science.abj8944

Biggin, A. J., Steinberger, B., Aubert, J., Suttie, N., Holme, R., Torsvik, T. H., ... Van Hinsbergen, D. J. (2012). Possible links between long-term geomagnetic variations and whole-mantle convection processes. *Nature Geoscience*, *5*(8), 526–533. doi: 10.1038/ngeo1521

Boehler, R. (1996). Melting temperature of the Earth's mantle and core: Earth's thermal structure. *Annual Review of Earth and Planetary Sciences*, *24*, 15–40. doi: 10.1146/annurev.earth.24.1.15

Bunge, H. P. (2005). Low plume excess temperature and high core heat flux inferred from non-adiabatic geotherms in internally heated mantle circulation models. *Physics of the Earth and Planetary Interiors*, *153*(1-3), 3–10. doi: 10.1016/j.pepi.2005.03.017

Burke, K., Steinberger, B., Torsvik, T. H., Smethurst, M. A. (2008). Plume Generation Zones at the margins of Large Low Shear Velocity Provinces on the core-mantle boundary. *Earth and Planetary Science Letters*, *265*(1-2), 49–60. doi: 10.1016/j.epsl.2007.09.042

Chen, J. (2016). Lower-mantle materials under pressure. *Science*, *351*(6269), 122–123. doi: 10.1126/science.aad7813

Christensen, U. R., Hofmann, A. W. (1994). Segregation of subducted oceanic crust in the convecting mantle. *Journal of Geophysical Research*, *99*(B10), 19,867–19,884. doi: 10.1029/93jb03403

Čížková, H., van den Berg, A. P., Spakman, W., Matyska, C. (2012). The viscosity of Earth's lower mantle inferred from sinking speed of subducted lithosphere. *Physics of the Earth and Planetary Interiors*, *200-201*, 56–62. doi: 10.1016/j.pepi.2012.02.010

Coltice, N., Schmalzl, J. (2006). Mixing times in the mantle of the early Earth derived from 2-D and 3-D numerical simulations of convection. *Geophysical Research Letters*, *33*(23), 5–8. doi: 10.1029/2006GL027707

Conrad, C. P., Steinberger, B., Torsvik, T. H. (2013). Stability of active mantle upwelling revealed by net characteristics of plate tectonics - supplementary. *Nature*, *498*, 479–482. doi: 10.1038/nature

Coppari, F., Smith, R. F., Wang, J., Millot, M., Kim, D., Rygg, J. R., … Duffy, T. S. (2021). Implications of the iron oxide phase transition on the interiors of rocky exoplanets. *Nature Geoscience*, *14*(3), 121–126. Retrieved from `http://dx.doi.org/10.1038/s41561-020-00684-y` doi: 10.1038/s41561-020-00684-y

Courtillot, V., Olson, P. (2007). Mantle plumes link magnetic superchrons to phanerozoic mass depletion events. *Earth and Planetary Science Letters*, *260*(3-4), 495–504. doi: 10.1016/j.epsl.2007.06.003

Crameri, F. (2018). Geodynamic diagnostics, scientific visualisation and StagLab 3.0. *Geoscientific Model Development*, *11*(6), 2541–2562. doi: 10.5194/gmd-11-2541-2018

Crameri, F., Tackley, P. J. (2014). Spontaneous development of arcuate single-sided subduction in global 3-D mantle convection models with a free surface. *Journal of Geophysical Research: Solid Earth*, *119*(7), 5921–5942. doi: 10.1002/2014JB010939

Dabrowski, M., Schmid, D. W., Podladchikov, Y. Y. (2012). A two-phase composite in simple shear: Effective mechanical anisotropy development and localization potential. *Journal of Geophysical Research: Solid Earth*, *117*(8), 3. doi: 10.1029/2012JB009183

Dannberg, J., Eilon, Z., Faul, U., Gasmöller, R., Moulik, P., Myhill, R. (2017). The importance of grain size to mantle dynamics and seismological observations. *Geochemistry Geophysics Geosystems*, *18*, 3034–3061. Retrieved from `10.1002/2016GC006787` doi: 10.1002/2017GC006944.Received

Davaille, A. (1999). Two-layer thermal convection in miscible viscous fluids. *Journal of Fluid Mechanics*, *379*, 223–253. doi: 10.1017/S0022112098003322

Davaille, A., Romanowicz, B. (2020). Deflating the LLSVPs: Bundles of Mantle Thermochemical Plumes Rather Than Thick Stagnant "Piles". *Tectonics*, *39*(10), 1–21. doi: 10.1029/2020TC006265

Davaille, A., Vatteville, J. (2005). On the transient nature of mantle plumes. *Geophysical Research Letters*, *32*(14), 1–4. doi: 10.1029/2005GL023029

Davies, G. F. (2007). Thermal Evolution of the Mantle. *Treatise on Geophysics*, *9*, 197–216. doi: 10.1016/B978-044452748-6.00145-0

Davies, G. F. (2008). Episodic layering of the early mantle by the 'basalt barrier' mechanism. *Earth and Planetary Science Letters*, *275*(3-4), 382–392. doi: 10

.1016/j.epsl.2008.08.036

de Montserrat, A., Faccenda, M., Pennacchionni, G. (2021). Extrinsic Anisotropy of Two-Phase Newtonian Aggregates : Fabric Characterization and Parameterization. *Journal of Geophysical Research: Solid Earth*, *126*(e2021JB022232).

Dziewonski, A. M., Lekic, V., Romanowicz, B. A. (2010). Mantle Anchor Structure: An argument for bottom up tectonics. *Earth and Planetary Science Letters*, *299*(1-2), 69–79. doi: 10.1016/j.epsl.2010.08.013

Farnetani, C. G. (1997). Excess temperature of mantle plumes: The role of chemical stratification across D. *Geophysical Research Letters*, *24*(13), 1583–1586. doi: 10.1029/97GL01548

Farnetani, C. G., Samuel, H. (2005). Beyond the thermal plume paradigm. *Geophysical Research Letters*, *32*(7), 1–4. doi: 10.1029/2005GL022360

Forte, A. M., Mitrovica, J. X. (1996). New inferences of mantle viscosity from joint inversion of long-wavelength mantle convection an post-glacial rebound data. *Geophysical Research Letters*, *23*(10), 1147–1150.

French, S. W., Romanowicz, B. (2015). Broad plumes rooted at the base of the Earth's mantle beneath major hotspots. *Nature*, *525*(7567), 95–99. doi: 10 .1038/nature14876

Frost, D. A., Avery, M. S., Buffett, B. A., Chidester, B. A., Deng, J., Dorfman, S. M., … Martin, J. F. (2022). Multidisciplinary Constraints on the Thermal-Chemical Boundary Between Earth's Core and Mantle. *Geochemistry, Geophysics, Geosystems*, *23*(3). doi: 10.1029/2021GC009764

Fuchs, L., Becker, T. W. (2019). Role of strain-dependent weakening memory on the style of mantle convection and plate boundary stability. *Geophysical Journal International*, *218*(1), 601–618. doi: 10.1093/gji/ggz167

Garnero, E. J., McNamara, A. K. (2008). Structure and Dynamics of Earth's Lower Mantle. *Science*, *320*(5876), 626–628. doi: 10.1126/science.1148028

Girard, J., Amulele, G., Farla, R., Mohiuddin, A., Karato, S. I. (2016). Shear deformation of bridgmanite and magnesiowüstite aggregates at lower mantle conditions. *Science*, *351*(6269), 144–147. doi: 10.1126/science.aad3113

Griffiths, R. W., Campbell, I. H. (1990). Stirring and structure in mantle starting plumes. *Earth and Planetary Science Letters*, *99*(1-2), 66–78. doi: 10.1016/0012-821X(90)90071-5

Gülcher, A. J. P., Ballmer, M. D., Tackley, P. J. (2021). Coupled dynamics and evolution of primordial and recycled heterogeneity in Earth's lower mantle. *Solid Earth*, *12*(9), 2087–2107. doi: 10.5194/se-12-2087-2021

Gülcher, A. J. P., Gebhardt, D. J., Ballmer, M. D., Tackley, P. J. (2020). Variable dynamic styles of primordial heterogeneity preservation in the Earth's lower mantle. *Earth and Planetary Sciences Letters*, *536*(116160). doi: 10.1016/j.epsl.2020.116160

Handy, M. R. (1994). Flow laws for rocks containing two non-linear viscous phases : a phenomenological approach. *Journal of Structural Geology*, *16*(3), 287–301.

Hassan, R., Flament, N., Gurnis, M., Bower, D. J., Müller, D. (2015). Provenance of plumes in global convection models. *Geochemistry Geophysics Geosystems*, *16*(1), 267–300. Retrieved from `https://doi.org/10.1002/2014GC005606` doi: 10.1002/2014GC005684.Key

Hernlund, J. W., Tackley, P. J. (2008). Modeling mantle convection in the spherical annulus. *Physics of the Earth and Planetary Interiors*, *171*(1-4), 48–54. doi: 10.1016/j.pepi.2008.07.037

Herzberg, C., Condie, K., Korenaga, J. (2010). Thermal history of the Earth and its petrological expression. *Earth and Planetary Science Letters*, *292*(1-2), 79–88. doi: 10.1016/j.epsl.2010.01.022

Herzberg, C., Rudnick, R. (2012). Formation of cratonic lithosphere: An integrated thermal and petrological model. *Lithos*, *149*, 4–15. doi: 10.1016/j.lithos.2012 .01.010

Hinkel, N. R., Timmes, F. X., Young, P. A., Pagano, M. D., Turnbull, M. C. (2014). Stellar abundances in the solar neighborhood: The hypatia catalog. *Astronomical Journal*, *148*(3). doi: 10.1088/0004-6256/148/3/54

Hirose, K., Morard, G., Sinmyo, R., Umemoto, K., Hernlund, J. W., Helffrich, G. R., Labrosse, S. (2017). Crystallization of silicon dioxide and compositional evolution of the Earth's core. *Nature*, *543*(7643), 99–102. doi: 10.1038/nature21367

Hirose, K., Sinmyo, R., Hernlund, J. W. (2017). Perovskite in Earth's deep interior. *Science*, *738*(November), 734–738. doi: 10.1126/science.aam8561

Howard, L. N. (1964). Thermal convection at high Rayleigh number. In H. Görtler (Ed.), *Applied mechanics. proceedings of 11th internaional congress* (pp. 1109–1115). Berlin: Springer. doi: 10.1017/s0004972700024965

Hwang, Y. K., Ritsema, J., van Keken, P. E., Goes, S., Styles, E. (2011). Wavefront healing renders deep plumes seismically invisible. *Geophysical Journal International*, *187*(1), 273–277. doi: 10.1111/j.1365-246X.2011.05173.x

Immoor, J., Miyagi, L., Liermann, H. P., Speziale, S., Schulze, K., Buchen, J., ... Marquardt, H. (2022). Weak cubic CaSiO3 perovskite in the Earth's mantle. *Nature*, *603*(7900), 276–279. doi: 10.1038/s41586-021-04378-2

Ito, E., Sato, H. (1991). Aseismicity in the lower mantle by superplasticity of the descending slab. *Nature*, *351*(6322), 140–141. doi: 10.1038/351140a0

Jeanloz, R., Morris, S. (1986). Temperature distribution int he crust and mantle. *Annual Review of Earth and Planetary Sciences*, *14*, 377–415.

Kaercher, P., Miyagi, L., Kanitpanyacharoen, W., Zepeda-Alarcon, E., Wang, Y., Parkinson, D., ... Wenk, H. R. (2016). Two-phase deformation of lower mantle mineral analogs. *Earth and Planetary Science Letters*, *456*, 134–145. Retrieved from `http://dx.doi.org/10.1016/j.epsl.2016.09.030` doi: 10.1016/j.epsl.2016.09.030

Karato, S., Riedel, M. R., Yuen, D. A. (2001). Rheological structure and deformation of subducted slabs in the mantle transition zone: Implications for mantle circulation and deep earthquakes. *Physics of the Earth and Planetary Interiors*, *127*(1-4), 83–108. doi: 10.1016/S0031-9201(01)00223-0

Koelemeijer, P., Deuss, A., Ritsema, J. (2017a). Density structure of Earth's lowermost mantle from Stoneley mode splitting observations. *Nature Communications*, *8*(May), 1–10. Retrieved from `http://dx.doi.org/10.1038/ncomms15241` doi: 10.1038/ncomms15241

Koelemeijer, P., Deuss, A., Ritsema, J. (2017b). Density structure of Earth's lowermost mantle from Stoneley mode splitting observations. *Nature Communications*, *8*(May), 1–10. Retrieved from `http://dx.doi.org/10.1038/ncomms15241` doi: 10.1038/ncomms15241

Kumagai, I., Davaille, A., Kurita, K., Stutzmann, E. (2008). Mantle plumes: Thin, fat, successful, or failing? Constraints to explain hot spot volcanism through time and space. *Geophysical Research Letters*, *35*(16). doi: 10.1029/2008GL035079

Labrosse, S. (2002). Hotspots, mantle plumes and core heat loss. *Earth and Planetary Science Letters*, *199*(1-2), 147–156. doi: 10.1016/S0012-821X(02)00537-X

Labrosse, S. (2003). Thermal and magnetic evolution of the Earth's core. *Physics of the Earth and Planetary Interiors*, *140*(1-3), 127–143. doi: 10.1016/j.pepi.2003.07.006

Larson, R. L., Olson, P. (1991). Mantle plumes control magnetic reversal frequency. *Earth and Planetary Science Letters*, *107*, 437–447.

Lau, H. C., Mitrovica, J. X., Austermann, J., Crawford, O., Al-Attar, D., Latychev, K. (2016). Inferences of mantle viscosity based on ice age data sets: Radial structure. *Journal of Geophysical Research: Solid Earth*, *121*(10), 6991–7012. doi: 10.1002/2016JB013043

Lay, T., Hernlund, J., Buffett, B. A. (2008). Core – mantle boundary heat flow. *Nature Geoscience*, *1*, 25–32.

Li, M., Zhong, S. (2017). The source location of mantle plumes from 3D spherical models of mantle convection. *Earth and Planetary Science Letters*, *478*, 47–57. Retrieved from `http://dx.doi.org/10.1016/j.epsl.2017.08.033` doi: 10.1016/j.epsl.2017.08.033

Li, Y., Deschamps, F., Tackley, P. J. (2014). The stability and structure of primordial reservoirs in the lower mantle: Insights from models of thermochemical convection in three-dimensional spherical geometry. *Geophysical Journal International*, *199*(2), 914–930. doi: 10.1093/gji/ggu295

Lin, S. C., Van Keken, P. E. (2006). Dynamics of thermochemical plumes: 2. Complexity of plume structures and its implications for mapping mantle plumes. *Geochemistry, Geophysics, Geosystems*, *7*(3). doi: 10.1029/2005GC001072

Massmeyer, A., Di Giuseppe, E., Davaille, A., Rolf, T., Tackley, P. J. (2013). Numerical simulation of thermal plumes in a Herschel-Bulkley fluid. *Journal of Non-Newtonian Fluid Mechanics*, *195*, 32–45. doi: 10.1016/j.jnnfm.2012.12.004

McKenzie, D. (1979). Finite deformation during fluid flow. *Geophys. J. R. astr. Soc.*, *58*, 689–715.

Mckenzie, D. P., Roberts, J. M., Weiss, N. O. (1974). Convection in the earth's mantle: Towards a numerical simulation. *Journal of Fluid Mechanics*, *62*(3), 465–538. doi: 10.1017/S0022112074000784

McNamara, A. K. (2019). A review of large low shear velocity provinces and ultra low velocity zones. *Tectonophysics*, *760*(August 2017), 199–220. doi: 10.1016/j.tecto.2018.04.015

Mitrovica, J. X., Forte, A. M. (2004). A new inference of mantle viscosity based upon joint inversion of convection and glacial isostatic adjustment data. *Earth and Planetary Science Letters*, *225*(1-2), 177–189. doi: 10.1016/j.epsl.2004.06.005

Miyagoshi, T., Kameyama, M., Ogawa, M. (2017). Extremely long transition phase of thermal convection in the mantle of massive super-Earths—. *Earth, Planets and Space*, *69*(46). doi: 10.1186/s40623-017-0630-6

Morgan, W. J. (1971). Convection plumes in the lower mantle. *Nature*, *230*(5288), 42–43. doi: 10.1038/230042a0

Mundl, A., Touboul, M., Jackson, M. G., Day, J. M., Kurz, M. D., Lekic, V., ... Walker, R. J. (2017). Tungsten-182 heterogeneity in modern ocean island basalts. *Science*, *356*(6333), 66–69. doi: 10.1126/science.aal4179

Nakagawa, T. (2020). A coupled core-mantle evolution: review and future prospects. *Progress in Earth and Planetary Science*, *7*(1). doi: 10.1186/s40645-020-00374-8

Nakagawa, T., Buffett, B. A. (2005). Mass transport mechanism between the upper and lower mantle in numerical simulations of thermochemical mantle convection with multicomponent phase changes. *Earth and Planetary Science Letters*, *230*(1-2), 11–27. doi: 10.1016/j.epsl.2004.11.005

Nakagawa, T., Tackley, P. J., Deschamps, F., Connolly, J. A. (2010). The influence of MORB and harzburgite composition on thermo-chemical mantle convection in a 3-D spherical shell with self-consistently calculated mineral physics. *Earth and Planetary Science Letters*, *296*(3-4), 403–412. doi: 10.1016/j.epsl.2010.05.026

Ogawa, M. (2003). Chemical stratification in a two-dimensional convecting mantle with magmatism and moving plates. *Journal of Geophysical Research*, *108*(B12). doi: 10.1029/2002jb002205

Olson, P. (1990). Hot spots, swells and mantle plumes. In M. P. Ryan (Ed.), *Magma transport and storage* (pp. 33–51). Wiley.

Olson, P., Schubert, G., Anderson, C. (1993). Structure of axisymmetric mantle plumes. *Journal of Geophysical Research*, *98*(B4), 6829–6844.

Peltier, W. R. (1996). Mantle viscosity and ice-age ice sheet topography. *Science*, *273*(5280), 1359–1364. doi: 10.1126/science.273.5280.1359

Putirka, K. D., Rarick, J. C. (2019). The composition and mineralogy of rocky exoplanets: A survey of >4000 stars from the Hypatia Catalog. *American Mineralogist*, *104*(6), 817–829. doi: 10.2138/am-2019-6787

Richards, M. A., Duncan, R. A., Courtillot, V. E. (1989). Flood basalts and hotspot tracks: Plume heads and tails. *Science*, *246*(4926), 103–107. doi: 10.1126/science.246.4926.103

Ritsema, J., Maguire, R., Cobden, L., Goes, S. (2021). Seismic Imaging of Deep Mantle Plumes. In H. Marquardt, M. D. Ballmer, S. Cottaar, J. G. Konter (Eds.), *Mantle convection and surface expressions* (pp. 353–369). AGU Monograph Series 263. doi: 10.1002/9781119528609.ch14

Schierjott, J., Rozel, A., Tackley, P. J. (2020). On the self-regulating effect of grain size evolution in mantle convection models: Application to thermochemical piles. *Solid Earth*, *11*(3), 959–982. doi: 10.5194/se-11-959-2020

Schubert, G., Masters, G., Olson, P., Tackley, P. (2004). Superplumes or plume clusters? *Physics of the Earth and Planetary Interiors*, *146*(1-2), 147–162. doi: 10.1016/j.pepi.2003.09.025

Sleep, N. H. (1990). Hotspots and mantle plumes: some phenomenology. *Journal of Geophysical Research*, *95*(B5), 6715–6736. doi: 10.1029/JB095iB05p06715

Solomatov, V. S., Reese, C. C. (2008). Grain size variations in the Earth's mantle and the evolution of primordial chemical heterogeneities. *Journal of Geophysical Research: Solid Earth*, *113*(7), 1–21. doi: 10.1029/2007JB005319

Spaargaren, R. J., Ballmer, M. D., Bower, D. J., Dorn, C., Tackley, P. J. (2020). The influence of bulk composition on the long-term interior-atmosphere evolution of terrestrial exoplanets. *Astronomy and Astrophysics*, *643*, 1–13. doi: 10.1051/0004-6361/202037632

Steinberger, B., Antretter, M. (2006). Conduit diameter and buoyant rising speed of mantle plumes: Implications for the motion of hot spots and shape of plume conduits. *Geochemistry, Geophysics, Geosystems*, *7*(11). doi: 10.1029/2006GC001409

Steinberger, B., Holme, R. (2008). Mantle flow models with core-mantle boundary constraints and chemical heterogeneities in the lowermost mantle. *Journal of Geophysical Research: Solid Earth*, *113*(5), 1–16. doi: 10.1029/2007JB005080

Stevenson, D. J. (2003). Planetary magnetic fields. *Earth and Planetary Science Letters*, *208*(1-2), 1–11. doi: 10.1016/S0012-821X(02)01126-3

Tackley, P. J. (2000a). Self-consistent generation of tectonic plates in three-dimensional mantle convection 1. pseudoplastic yielding. *Geochemistry, Geophysics, Geosystems*, *1*(1), 9–22. doi: 10.1016/S0012-821X(98)00029-6

Tackley, P. J. (2000b). Self-consistent generation of tectonic plates in time-dependent, three-dimensional mantle convection simulations 2. strain weakening and asthenosphere. *Geochemistry, Geophysics, Geosystems*, *1*. doi: 10.1029/2000gc000036

Tackley, P. J. (2008). Modelling compressible mantle convection with large viscosity contrasts in a three-dimensional spherical shell using the yin-yang grid. *Physics of the Earth and Planetary Interiors*, *171*(1-4), 7–18. doi: 10.1016/j.pepi.2008.08.005

Tackley, P. J. (2012). Dynamics and evolution of the deep mantle resulting from thermal, chemical, phase and melting effects. *Earth-Science Reviews*, *110*(1-4), 1–25. doi: 10.1016/j.earscirev.2011.10.001

Tackley, P. J., Ammann, M. W., Brodholt, J. P., Dobson, D. P., Valencia, D. (2013). Mantle dynamics in super-Earths: Post-perovskite rheology and self-regulation of viscosity. *Icarus*, *225*(1), 50–61. doi: 10.1016/j.icarus.2013.03.013

Thielmann, M., Golabek, G. J., Marquardt, H. (2020). Ferropericlase control of lower mantle rheology: Impact of phase morphology. *Geochemistry, Geophysics, Geosystems*, *21*(e2019GC008688). doi: 10.1029/2019gc008688

Torsvik, T. H., Burke, K., Steinberger, B., Webb, S. J., Ashwal, L. D. (2010). Diamonds sampled by plumes from the core-mantle boundary. *Nature*, *466*(7304), 352–355. Retrieved from `http://dx.doi.org/10.1038/nature09216` doi: 10.1038/nature09216

Torsvik, T. H., Svensen, H. H., Steinberger, B., Royer, D. L., Jerram, D. A., Jones, M. T., Domeier, M. (2021). Connecting the Deep Earth and the Atmosphere. In H. Marquardt, M. D. Ballmer, S. Cottaar, J. G. Konter (Eds.), *Mantle convection and surface expression* (pp. 413–453). Geophysical Monography Series 263. doi: 10.1002/9781119528609.ch16

Torsvik, T. H., Van Der Voo, R., Doubrovine, P. V., Burke, K., Steinberger, B., Ashwal, L. D., . . . Bull, A. L. (2014). Deep mantle structure as a reference frame for movements in and on the Earth. *Proceedings of the National Academy of Sciences of the United States of America*, *111*(24), 8735–8740. doi: 10.1073/pnas.1318135111

Tschauner, O., Huang, S., Yang, S., Humayun, M., Liu, W. (2021). Discovery of davemaoite, CaSiO 3 -perovskite, as a mineral from the lower mantle. *Science*, *894*(November), 891–894.

van Hunen, J., Zhong, S., Shapiro, N. M., Ritzwoller, M. H. (2005). New evidence for dislocation creep from 3-D geodynamic modeling of the Pacific upper mantle structure. *Earth and Planetary Science Letters*, *238*(1-2), 146–155. doi: 10.1016/j.epsl.2005.07.006

van Keken, P. E. (1997). Evolution of starting mantle plumes: a comparison between numerical and laboratory models. *Earth and Planetary Science Letters*, *148*(97).

Wicks, J. K., Duffy, T. S. (2016). Crystal Structures of Minerals in the Lower Mantle. *Deep Earth: Physics and Chemistry of the Lower Mantle and Core*, 69–87. doi: 10.1002/9781118992487.ch6

Wilson, J. T. (1963). *A possible origin of the Hawaiian Islands* (Vol. 51) (No. 3). doi: 10.1139/cjes-2014-0036

Wolfe, C. J., Solomon, S. C., Laske, G., Collins, J. A., Detrick, R. S., Orcutt, J. A., . . . Hauri, E. H. (2009). Mantle shear-wave velocity structure beneath the Hawaiian hot spot. *Science*, *326*(5958), 1388–1390. doi: 10.1126/science.1180165

Xie, S., Tackley, P. J. (2004). Evolution of U-Pb and Sm-Nd systems in numerical models of mantle convection and plate tectonics. *Journal of Geophysical Research: Solid Earth*, *109*(11), 1–22. doi: 10.1029/2004JB003176

Xu, W., Lithgow-Bertelloni, C., Stixrude, L., Ritsema, J. (2008). The effect of bulk composition and temperature on mantle seismic structure. *Earth and Planetary Science Letters*, *275*(1-2), 70–79. doi: 10.1016/j.epsl.2008.08.012

Yamazaki, D., Inoue, T., Okamoto, M., Irifune, T. (2005). Grain growth kinetics of ringwoodite and its implication for rheology of the subducting slab. *Earth and Planetary Science Letters*, *236*(3-4), 871–881. doi: 10.1016/j.epsl.2005.06.005

Yamazaki, D., Karato, S. I. (2001). Some mineral physics constraints on the rheology and geothermal structure of Earth's lower mantle. *American Mineralogist*, *86*(4), 385–391. doi: 10.2138/am-2001-0401

Yan, J., Ballmer, M. D., Tackley, P. J. (2020). The evolution and distribution of recycled oceanic crust in the Earth's mantle: Insight from geodynamic models. *Earth and Planetary Science Letters*, *537*(March). doi: 10.1016/j.epsl.2020.116171